Hypoeutectic liquid metal printing of two-dimensional indium gallium oxide transistors

2 Simon A. Agnew, Anand P. Tiwari, Samuel W. Ong, Md Saifur Rahman, and William J. Scheideler*

3

1

- 4 Thayer School of Engineering
- 5 Dartmouth College, Hanover, NH 03755, United States
- 6 E-mail: william.j.scheideler@dartmouth.edu

7

- 8 Keywords: liquid metals, 2D oxides, transparent electronics, thin film transistors, flexible
- 9 transistors

10

11 Two-dimensional (2D) native surface oxides formed on low melting temperature metals such as indium and gallium offer unique opportunities for fabricating high-performance flexible 12 13 electronics and optoelectronics based on a new class of liquid metal printing (LMP). An inherent 14 property of these Cabrera-Mott 2D oxides is their suboxide nature (e.g. In₂O_{3-x}), which leads high mobility LMP semiconductors to exhibit high electron concentrations ($n_e > 10^{19}$ cm⁻³) limiting 15 electrostatic control. Binary alloying of the molten precursor can produce doped, ternary metal 16 oxides such as In-X-O with enhanced electronic performance and greater bias-stress stability, 17 though this approach demands deeper understanding of the native oxides of alloys. This work 18 19 presents an approach for hypoeutectic rapid LMP of crystalline InGaO_x (IGO) at ultralow process 20 temperatures (180 °C) beyond the state of the art to fabricate transistors with 10X steeper subthreshold slope and high mobility (~ 18 cm²/Vs). Detailed characterization of IGO crystallinity, 21 22 composition, and morphology, as well as measurements of its electronic density of states (DOS), 23 show the impact of Ga-doping and reveal the limits of doping induced amorphization from 24 hypoeutectic precursors. The ultralow process temperatures and compatibility with high-k Al₂O₃ 25 dielectrics shown here indicate potential for 2D IGO to drive low-power flexible transparent

27

26

electronics.

1. Introduction

Transparent conductive oxides (TCOs) are a vital material for the electronics industry, with applications ranging from photovoltaics, $^{[1]}$ chemical sensing, $^{[2,3]}$ displays, $^{[4,5]}$ and flexible thin film circuits. $^{[6-9]}$ Indium oxide (InO_x) is a wide band gap n-type semiconductor that exhibits high free electron concentrations ($n_e > 10^{18}$ cm⁻³) and high electron mobilities on the order of 100 cm² V⁻¹ s⁻¹ for crystalline sputtered films. $^{[10]}$ Due to their overlapping spherical s orbitals which comprise the conduction band minimum, post-transition metals are ideal dopants as they do not compromise the high isotropic mobility seen in pure InO_x . $^{[11]}$ Doping with post-transition metals to create ternary (e.g., ITO, IZO) and quaternary metal oxides (e.g., IGZO, ITZO) can suppress or enhance the free electron concentration, achieving desirable performance depending on the application. Indium tin oxide (ITO) is highly conductive ($n_e > 10^{20}$ cm⁻³) and is widely used as transparent electrodes in optoelectronics. $^{[12,13]}$ Amorphous indium-gallium-zinc oxide (IGZO) has been commercialized as a semiconducting channel in thin film transistors (TFTs) for modern display technologies due to its stability and favorable electron mobilities. $^{[4,14]}$

Most processes for fabricating TCOs require vacuum technologies such as sputtering, with throughputs that are limited by the batchwise manufacturing process as well as the high capital expenditure of vacuum tools. Non-vacuum methods such as sol-gel synthesis of metal oxides often require high process temperatures above 300 °C for full chemical conversion.^[15] Roll-to-roll compatible processes that can be operated in open air and at temperatures compatible with flexible, plastic substrates (< 250 °C) present a breakthrough in throughput and cost reduction for flexible devices and systems. Liquid metal printing (LMP) has gained attention as a scalable, open-air process that can rapidly deposit polycrystalline films with thicknesses on the order of several nanometers.^[16] At low temperatures, the surface oxidation of metals can be described by the Cabrera-Mott oxidation theory.^[17] A nm-scale surface oxide spontaneously forms on the surface of the liquid metal in air, which is easily transferred to a target substrate via van der Waals forces that are stronger than the weak adhesion between the oxide film and the liquid metal.^[18] The exfoliation of the oxide can be achieved either by touch-printing the target substrate to the liquid metal droplet, squeeze printing, or rolling the droplet across the substrate. Liquid metal printing has been shown to be an efficient, scalable method for depositing metal oxides at temperatures just above the melting point of the donor metal alloy droplet (e.g. 157 °C for In, 232 °C for Sn), enabling compatibility with large-area deposition on plastic substrates.^[16]

We have previously reported that LMP InO_x TFTs printed at low temperatures exhibit very high free electron concentrations ($n_e > 10^{19}$ cm⁻³), leading to depletion mode device operation with large negative turn on voltages (Von).[19] Previous studies have shown for vacuum-based and solution-processed films that Ga-doping to form an In-rich ternary indium-gallium oxide (IGO) can improve off-state behavior and lead to near-enhancement mode operation via a reduction in the free electron concentration, notably via reduced oxygen vacancies.^[20–22] Achieving lower off currents and steeper switching in LMP InO_x films could be accomplished via doping with Ga. When liquid metal printing with an alloy, the composition of the surface oxide of the liquid metal droplet is distinct from the composition of the liquid metal alloy. In many cases, the more thermodynamically favored oxide (greater enthalpy of formation) tends to dominate. Eutectic gallium-indium (eGaIn) consists of 85.8 at. % Ga but forms a surface oxide almost entirely composed of GaO_x as shown several recent works.^[23–25] The same Ga dominance occurs in other Ga-rich alloys such as galinstan, a Ga-In-Sn alloy. [26] The current popular explanation for this dominance is that the metal oxide with the largest reduction in Gibbs free energy of formation (ΔG_f) will primarily compose the surface oxide. [18,25,27] Other metal oxides such as HfO₂ and Al₂O₃ have been fabricated by exploiting this dominating thermodynamic effect. It is thus difficult to achieve a ternary indium gallium oxide (IGO) film by liquid metal printing with near-eutectic InGa alloys due to the suppression of the formation of InO_x at the surface.

We present the successful introduction of Ga as a dopant in LMP InO_x films by rapidly printing large area (> $10 \text{ cm}^2/\text{s}$) films with extremely hypoeutectic InGa alloys. We have characterized the relationship between the liquid metal alloy composition and the resulting surface oxide stoichiometry, highlighting the extremely strong effect of Ga surface enrichment. The effects of Ga doping on the crystallinity, optical band gap, and film conductivity were investigated. Most notably, higher doping concentrations of Ga result in less conductive films. We have successfully introduced Ga as a dopant below the amorphization limit to produce semiconducting crystalline IGO with a similar morphology to pure LMP InO_x . We have fabricated ~ 8 at. % Ga IGO TFTs at $180 \, ^{\circ}$ C with the lowest Ga concentration alloy (0.001 wt. % Ga) and show a remarkable improvement in V_{on} (up to $+50 \, \text{V}$ higher) and $10 \, \text{X}$ steeper switching with mobilities up to $\sim 18 \, \text{cm}^2 \text{V}^{-1} \text{s}^{-1}$. We further improve the switching capabilities of LMP IGO by fabricating TFTs on high-k Al_2O_3 substrates to achieve subthreshold slopes as low as $210 \, \text{mV/dec}$.

2. Results and Discussion

1

2

3

8

9

10

11

12

13

14

15

16

17

18

19

20

21

22

23

24

25

26

27

28

29

30

31

This study implements the method of roller-based continuous liquid metal printing (CLMP) developed in our previous work^[28,29] to deposit large area Ga-doped InO_x using InGa liquid metal alloys. As seen in Figure 1a, the target substrate (plasma-treated to promote oxide adhesion) is heated to above the melting temperature of the donor metal, and a silicone roller is used to translate the liquid metal meniscus across the target substrate, depositing the metal oxide along the path of the liquid metal. This roller-based implementation of liquid metal printing presents an easily scalable, low temperature, open-air method for roll-to-roll deposition of metal oxides. Due to the spontaneous nature of surface oxidation, CLMP can be operated > 20 cm/s and still yield continuous, high-quality metal oxide films requiring no post annealing. Successive metal oxide layers can be printed using the same method after removing residual liquid metal with isopropanol and optionally treating the substrate with surface plasma. See Experimental Methods for more details on the CLMP process and alloy preparation.

As discussed previously, Ga-based liquid metal alloys can often exhibit surface oxides dominated by GaO_x. The spontaneous Cabrera-Mott oxidation process is thermodynamically driven towards surface oxides composed of majority Ga given the lower redox potential of Ga. [30] Figure 1b illustrates this phenomenon of surface segregation of Ga in the oxide skin of the liquid metal alloy. In order to achieve control of the Ga content in the oxide using In-rich InGa alloys, hypoeutectic alloys were created with Ga concentrations as low as 10 ppm. To elucidate the limit of this oxide dominance effect, X-ray photoelectron spectroscopy (XPS) was performed on IGO films printed with various InGa alloys at 180 °C (Figure 1c). An example wide survey XPS scan for an IGO film is shown in Figure S1. The effect of surface domination of Ga is shown to be extreme, with ~90 at. % Ga in the oxide when printing with a 1 wt. % Ga alloy. Further reduction of the Ga content in the alloy still results in a significant "over-representation" of Ga in the oxide, over several orders of magnitude greater than in the alloy. For example, at 0.001 wt. % Ga in the liquid metal alloy, the resulting oxide has ~8 at. % Ga, enriched by a factor of almost 10,000X compared with the precursor. Similar over-representations of Ga of over 1000X were shown by Guo et al. in their recent work.^[31] The high resolution sub-nm depth profiling of eGaIn surface oxides reported by Martin and Thuo would also suggest that the distribution of GaO_x in our 2D IGO films should be expected to be non-uniform, with the potential for forming an In-rich inner

- 1 surface oxide and Ga-rich outer surface^[30]. In such a scenario, the In-rich surface would form the
- 2 transistor back channel and the Ga-rich surface would constitute the dielectric interface.

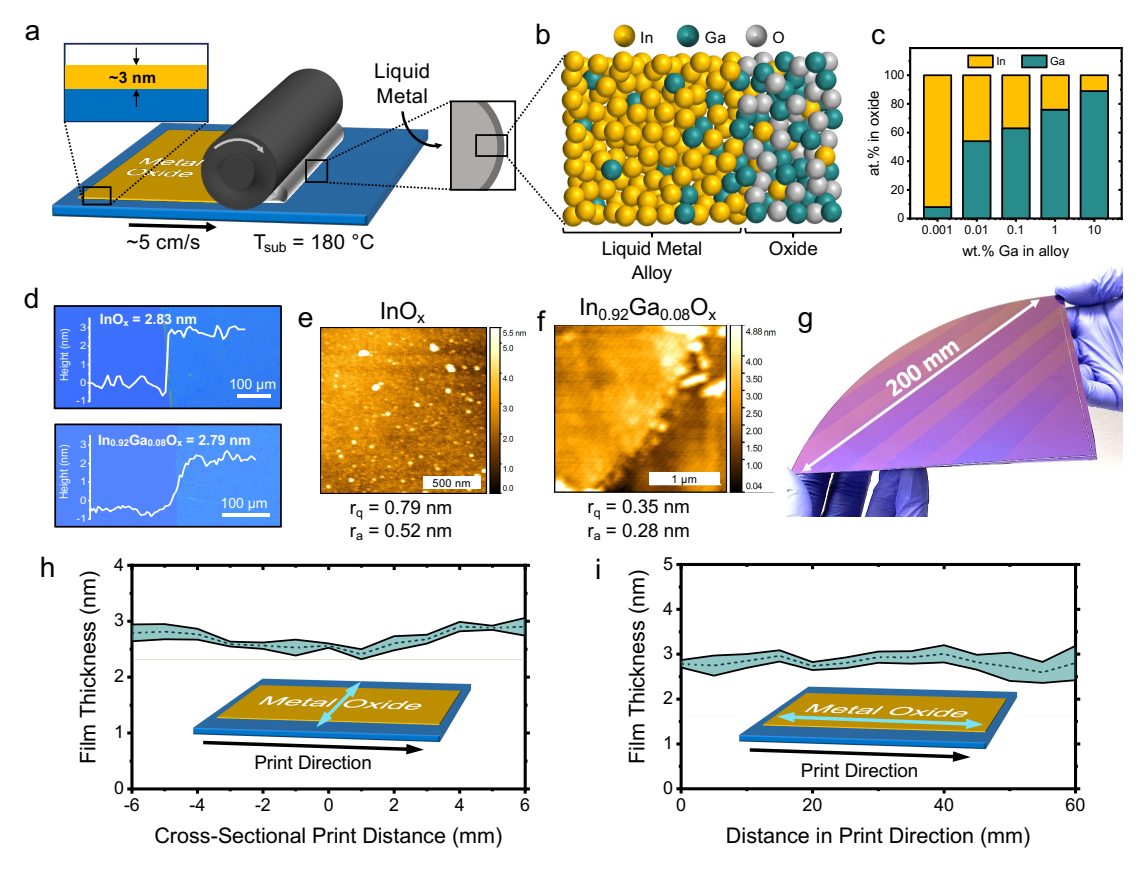


Figure 1: (a) Schematic of roller-based CLMP process. (b) Illustration of surface oxide domination of Ga in liquid InGa alloys. (c) XPS quantification of resulting surface oxide stoichiometry when printing with alloys of varying Ga content at 180 °C. (d) AFM height profiles of single layer InO_x and $InGaO_x$ printed at 180 °C overlayed on optical microscope images showing films. (e) AFM scan of InO_x surface. (f) AFM scan of $InO_{.92}Ga_{0.08}O_x$ surface. (g) Demonstration of capability of rapid, large-area CLMP deposition of IGO at the > 100 mm scale. (h,i) Thickness mapping of the IGO film perpendicular (cross-web) and parallel (down-web) to the print direction, respectively.

To evaluate the impact of Ga-doping on film morphology, atomic force microscopy (AFM) was performed to analyze the nano-scale thickness of the CLMP oxides. **Figure 1d** shows height profiles of single layer InO_x and In_{0.92}Ga_{0.08}O_x printed at 180 °C superimposed on optical microscope images, with film thicknesses of 2.83 and 2.79 nm, respectively. The inclusion of Ga in the film does not significantly change the printed oxide thickness compared to pure InO_x at the identical process temperature and roller speed (5 cm/s). We also noted in our previous work that pure InO_x and GaO_x films produced via CLMP at the same process conditions show very similar film thicknesses.^[29] It would therefore be expected that the ternary IGO should not significantly differ in thickness versus pure InO_x. The oxide films are very smooth, with sub-nm surface

roughness values for both InO_x (**Figure 1e**) and IGO (**Figure 1f**) comparable or even smoother than atomic layer deposited (ALD) IGO films. [32] It is worth noting that the IGO film showed lower surface roughness values ($r_a = 0.28$ nm) and a visibly smoother appearance than the InO_x film. The capability of fabricating highly uniform, continuous oxide films with the CLMP method is highlighted in **Figure 1g**, where 105 cm² of oxide was printed in 4 s. Additionally, the large-area thickness uniformity for an IGO sample printed at ~5 cm/s was mapped in the perpendicular and parallel directions with respect to the print direction (cross-web and down-web directions in roll-to-roll manufacturing terminology, respectively). **Figure 1h** shows that the edges of the printed film are slightly thicker than the center of the film, perhaps due to edge folding of multiple layers of oxide. **Figure 1i** illustrates the uniformity of the film thickness in the print direction, with an average film thickness standard deviation of ~0.2 nm. Though measured over a different length scale, this standard deviation is similar to the RMS surface roughness of 0.28 nm obtained from the AFM scans.

To further characterize the nanoscale morphology, X-ray diffraction (XRD) was performed to analyze the crystallinity of CLMP IGO films. As seen in Figure 2a, the In_{0.92}Ga_{0.08}O_x film exhibited the characteristic (222) and (400) peaks matching cubic bixbyite In₂O₃,^[33] similar to control samples of undoped InO_x printed under the same conditions. Scherrer-Debye estimates of grain size for both IGO and the pure InO_x were approximately 5 nm, however we note that this method underestimates the actual grain size in these 2D oxide films that typically exhibit platelike rather than spherical grains^[28]. No α-Ga₂O₃ or β-Ga₂O₃ peaks were detected in any of the IGO films, and all IGO films except the 8 at. % Ga film were amorphous. This would suggest the amorphization limit for CLMP IGO films at the 180 °C process temperature is likely above 10 at. % Ga. The higher intensity of the (222) peak in pure InO_x indicates the preference for grain growth in the (222) direction rather than the (400) direction. The crystalline IGO sample showed little preference as the ratio intensities of the (222) and (400) peaks are nearly identical. We have shown in previous work that more stoichiometric InO_x films printed at higher temperatures (e.g. 240 °C) show a stronger (400) peak relative to the (222) peak, so the higher (400) intensity in the crystalline IGO film matches our hypothesis of a reduction in oxygen vacancies from the inclusion of Ga.^[28] These highly crystalline morphologies achieved by the CLMP method at the low temperature of 180 °C present a remarkable improvement in the necessary process temperature to achieve crystalline oxide films, especially considering no post annealing was performed. Reported solution

processed InO_x-based films require annealing above at least 350 °C to achieve crystalline phases, $^{[34-36]}$ highlighting the > 150 °C reduction in process temperature necessary to deposit crystalline thin films with CLMP.

The optical properties of IGO films of varying Ga content printed at 180 °C were investigated. Both InO_x and IGO films showed excellent optical transmission above 98 % in the visible range (See **Figure S2**), typical of such 2D oxide films. Absorption spectra were collected for various IGO films to determine the optical band gaps via direct band gap Tauc plot fits (**Figure 2b**). A direct bandgap fit is chosen for In₂O₃ in light of previous studies^[37] showing that strong optical absorption above 3.6 eV results from a direct transition from well below the valence band maximum due to the dipole-forbidden nature of lower energy absorption near the fundamental bandgap of 2.9eV. A monotonic trend of optical band gap versus Ga content is seen in **Figure S3**, ranging from 3.55 eV for pure InO_x up to 4.09 eV for In_{0.1}Ga_{0.9}O_x. The high optical transparency of these oxides is due to both their wide band gaps (> 3 eV) and nm-scale thickness.

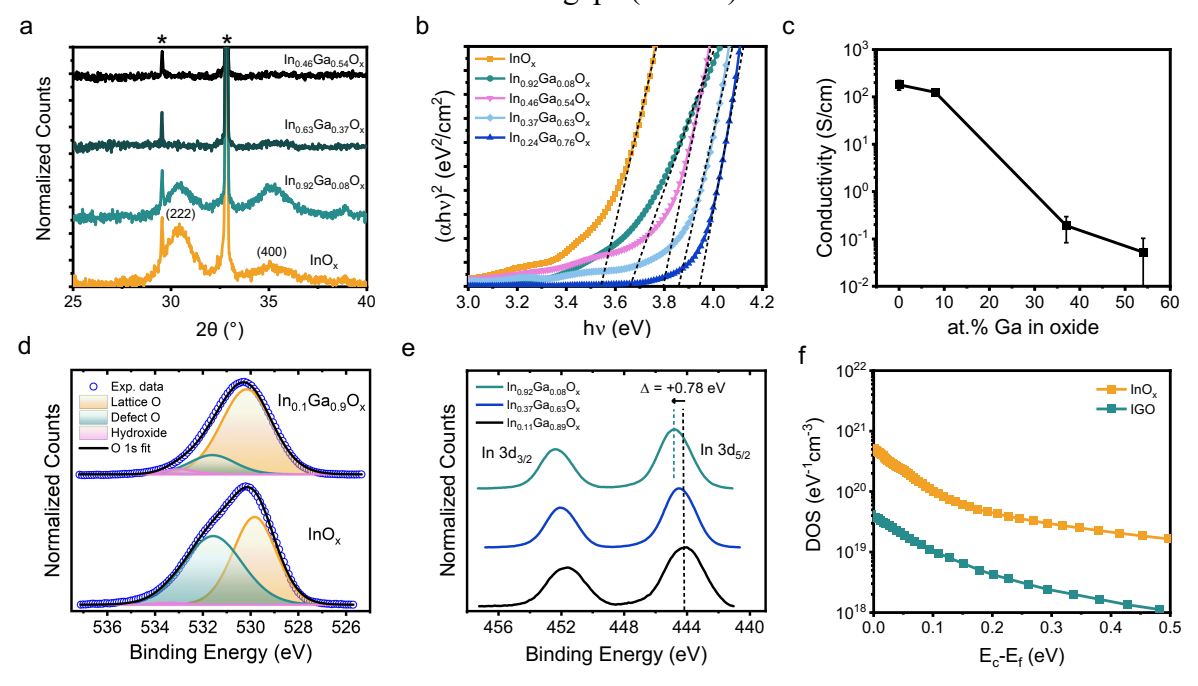


Figure 2: (a) XRD spectra of InO_x and IGO films printed at 180 °C with no post annealing (* denotes Si substrate peak). (b) Direct band gap Tauc plot fit of oxides with varying Ga content. (c) Film conductivity versus Ga content. (d) O 1s XPS comparison between pure InO_x and IGO. (e) In 3d XPS comparison for IGO films of varying Ga content. (f) Extracted electronic DOS distribution for InO_x and In_{0.92}Ga_{0.08}O_x.

The electrical properties and composition of the IGO films reveal the role of Ga doping in facilitating greater electrostatic control of LMP 2D oxides. The free electron concentrations of InO_x can be over 10^{20} cm⁻³ due to the presence of excess oxygen vacancies acting as shallow electron donors in sub-stoichiometric In_2O_{3-x} . [38,39] Control of the oxygen partial pressure in the

fabrication process of vacuum-based deposition methods can aid in the reduction of oxygen vacancies if lower free electron concentrations are desired. [40] Introducing Ga as a dopant in InO_x films is known to reduce the oxygen vacancy distribution due to the higher bond strength of Ga-O versus In-O, which effectively "pulls" more oxygen into the film. [41-43] It would be expected that an IGO film with higher Ga content would exhibit a lower conductivity due to a reduction in the free electron concentration. It is thus unsurprising to see in Figure 2c that pure InO_x films show rather high conductivities on the order of 10^2 S/cm given the low processing temperature of 180 °C, whereas IGO films containing just over 50 at. % Ga exhibit conductivities over 1000X lower due to a reduction in oxygen vacancy defects. XPS was used to evaluate the presence of oxygen vacancies in the films to elucidate the impact of Ga doping on electrical performance. Figure 2d shows the O 1s peak for pure InO_x and an IGO film containing the majority of Ga. The contribution from oxygen vacancy defects, shown in green, is greatly suppressed in the IGO film. For example, the inclusion of Ga (In_{0.1}Ga_{0.9}O_x) suppressed the oxygen-deficient defect bonding peak by over 3X compared to that of pure InO_x. The reduction in free electron concentrations in higher Ga content films is supported by the shift in the binding energy of the In $3d_{5/2}$ peak in Figure 2e. Past studies of In₂O₃ have established that a higher binding energy observed for core-level peaks such as the In $3d_{5/2}$ correlates strongly to increase (closer to vacuum) in the Fermi level (E_f)^[44].

To further elucidate the effect of Ga on the semiconducting properties of IGO, the total sub-gap electronic density of states (DOS) distribution was extracted for pure InO_x and 8 at. % IGO (**Figure 2f**) using temperature-dependent transfer measurements. The IGO devices displayed stable transfer characteristics with minimal threshold and turn-on-voltage shifts across the range of measurement temperatures (**Figure S4**), highlighting their stability in higher temperature operating environments. The DOS extraction by this method produces a sum total of the DOS of the bulk states in the channel as well as interface states at the front- or back-channel surfaces. The characteristic biexponential distribution of localized electronic states for a disordered semiconductor was observed for both materials, with around a 10X overall reduction in the DOS for IGO versus pure InO_x. These exponential distributions are often described as a linear superposition of exponential "tail states" close to the band edge, and exponential "deep states" further into the band gap (See **Figures S5 & S6** for exponential fitting). The IGO deep state density is at least 10X lower than that of pure InO_x, providing evidence that the inclusion of Ga reduces the concentration of oxygen vacancy defects. The DOS near the conduction band

minimum is also decreased by approximately 10X as a result of Ga-doping. The origins of the states near the CBM have been previously attributed to the variation of In-O-metal bond angles and variation in the coordination of In atoms^[46]. Theoretical work by Medvedeva, et al.^[47] has shown that Ga incorporation into In-X-O introduces significant changes to local order, for example, reducing the average bond lengths of In-O and increasing the fraction of fully coordinated In atoms (In-O bonding). Both these factors could reduce the DOS near the CBM for the IGO compositions utilized in the present study. The reduction in deep state trap density is linked directly to the improved subthreshold slopes and steeper device switching^[48] as demonstrated by the device characteristics shown in **Figure 3**. Additionally, analysis of the Urbach tails from the absorption spectra of IGO films show a decrease in the Urbach energy E_U with

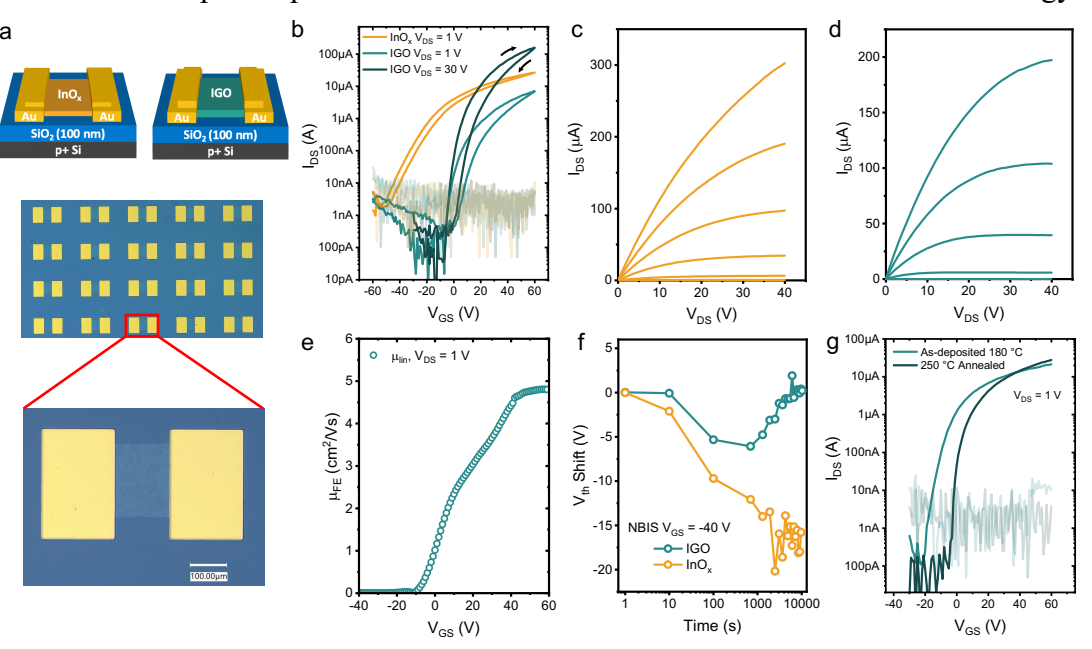


Figure 3: (a) Device architecture and optical microscope image of TFT. (b) Representative transfer characteristic comparison between pure InO_x and IGO devices. (c,d) Output curves for pure InO_x and IGO devices, respectively (V_{GS} swept from -20 to 40 V in 16 V increments). (e) Representative incremental linear field effect mobility of IGO devices. (f) NBIS shift in threshold voltage over 3 hours of -40 V gate biasing for pure InO_x and IGO devices. (g) Representative transfer comparison between unannealed IGO devices and after 250 °C anneal for 2 h.

increasing Ga content, indicating a decrease in optically active subgap defects (Figure S7).

Bottom gate, top contact TFTs were fabricated using CLMP InO_x and In_{0.92}Ga_{0.08}O_x printed at 180 °C on 100 nm SiO₂ substrates. Due to the lower conductivity of the IGO film, two layers were printed successively as the channel material whereas only a single layer was printed for the pure InO_x devices. **Figure 3a** shows device architectures and an optical microscope image of the InO_x TFTs. Transfer characteristics of the InO_x versus IGO devices are shown in **Figure 3b**. The pure InO_x channel devices require large negative gate biases to fully deplete the channel, with

average turn on voltages (V_{on}) below -50 V. The IGO devices show a remarkable improvement in V_{on} , with an average positive shift of 32.2 \pm 9.6 V. Several devices showed near-enhancement mode operation, with V_{on} close to 0 V. As predicted from the DOS extraction, IGO devices show much steeper switching with a 2X average reduction in subthreshold slope over that of pure InO_x devices. The champion IGO device exhibited a linear mobility of 17.8 cm²/Vs and a subthreshold slope of 422 mV/dec. Figures 3c and 3d show representative output characteristics of InO_x and IGO devices, respectively. The IGO devices showed enhanced current saturation but slightly lower currents due to the reduced conductivity of the channel following the introduction of Ga as a dopant and significantly lower gate overdrive voltage from the positively shifted threshold voltage. Figure 3e shows the extracted incremental linear mobility μ_{lin} for an IGO device using

$$\mu_{\text{lin}} = \frac{L}{WC_{\text{ox}}V_{\text{DS}}} \frac{\partial I_{\text{DS}}}{\partial V_{\text{GS}}}$$
 (1)

where W/L is the device aspect ratio, C_{ox} is the areal gate capacitance, and V_{DS} is the drain to source voltage. The incremental mobility is shown to plateau above an applied gate field of ~1.5 MV/cm. The multiple trap and release (MTR) mobility model for disordered semiconductors defines the carrier mobility as a function of the ratio between n_{free} , the number of electrons in delocalized states above the mobility edge and the total electronic states, including the localized trap states n_{trap} within the band gap according to^[49]

$$\mu_{eff} \propto \frac{n_{free}}{n_{free} + n_{trap}} \tag{3}$$

As the applied vertical gate field increases, the Fermi level in the device moves closer to the conduction band edge and this fraction of free carriers to total carriers saturates. As the fraction of free carriers to total carriers saturates (approaches 1), the incremental mobility reaches its peak value in the on-state, which is achieved in the IGO TFTs despite their positively shifted turn on voltage relative to pure InO_x .

Bias stress instability is a known issue for metal oxide TFTs used as active switching devices in displays, as threshold voltage (V_{th}) stability is critical to ensure minimal variation of operating currents supplied to pixel elements.^[50] Negative bias voltages and illumination stress both cause significant shifting of V_{th} exacerbated by the presence of oxygen vacancies as well as adsorbed H_2O and electron trapping at the channel interfaces.^[43,51–54] Hennek *et al.* postulate that dopants with metal oxide lattice enthalpies (ΔH_L) larger than In (\sim 7500 kJ mol⁻¹), such as Ga

(~9500 kJ mol⁻¹) or Al can effectively act as oxygen "getter" dopants, reducing oxygen vacancies. [43] Doping with Ga has shown to reduce the instability of metal oxides, most notably in the improved stress stability of IGZO, which has allowed its commercialization as TFT channel materials in displays. [55-57] Negative bias illumination stress (NBIS) testing was performed on InO_x and IGO devices with a negative bias of -40 V applied to the gate. After 10⁴ s, the shift in V_{th} was shown to be negligible in IGO devices whereas a negative shift of more than 15 V occurred in pure InO_x devices (Figure 3f). The non-monotonic shift in threshold voltage observed for negatively stressed IGO devices is proposed to derive from the competing positive influence of the unpassivated back-channel interface traps resulting from exposure to moisture^[58] and ionization of oxygen vacancy defects in the bulk of these films. This advancement in bias stress stability of the ternary IGO is expected given the reported effects of doping with a metal exhibiting higher oxide bond strengths. The superior stability of IGO over pure InO_x in these devices without passivating layers suggests even further stability if integrated into encapsulated devices. The improved stability shown for IGO devices is also important given this technology's amenability to roll-to-roll based fabrication and flexible form factors for which effective encapsulation strategies are more limited due to rigidity of glass and some other encapsulation materials.

1

2

3

4

5

6

7

8

9

10

11

12

13

14

15

16

17

18

19

20

It is worth highlighting that all the films and devices presented thus far were printed at 180 °C. It is remarkable that crystalline films are achieved at such a low process temperature and short process time scales (< 5 s), and that near-enhancement mode operation devices with mobilities up to 17.8 cm²/Vs can be fabricated without requiring additional postannealing. To explore further

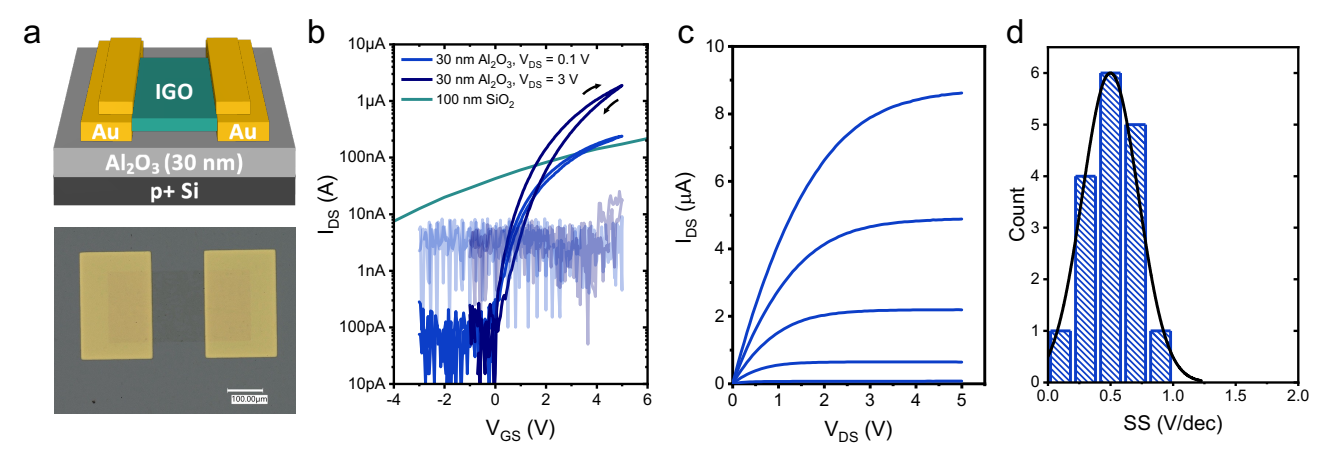


Figure 4: (a) Device architecture and optical microscope image of TFT on 30 nm Al₂O₃ dielectric. (b) Representative transfer characteristic comparison between IGO on 100 nm SiO₂ and 30 nm Al₂O₃. (c) Output curves for IGO on 30 nm Al₂O₃ (V_{GS} swept from -2 to 4 V in 1 V increments). (d) Histogram of subthreshold slopes extracted from IGO transfer curves.

improvement of electrical performance, IGO devices were subjected to a 250 °C postanneal in air.

Annealed devices showed an average 5X improvement in subthreshold slope and μ_{lin} up to 22.7 cm²/Vs. The off current was further suppressed by annealing, with I_{on}/I_{off} ratios up to 10⁷.

Enhancement-mode operation was achieved in some devices with V_{on} above 0 V (**Figure 3g**). **Table 1** shows a summary of these device performance parameters, noting average values, standard deviation, and the maxima. We note that for these post-annealed devices treated at 250

over sol-gel methods that require temperatures often exceeding 350 °C for postannealing steps. [20,41]

C, the compatibility with flexible substrates such as polyimide is still maintained, an advantage

Increasing the gate oxide capacitance with a thinner, high-k dielectric can increase the electrostatic control over the device, allowing for steeper switching and low voltage operation, which is attractive for low-power applications. ~30 nm Al₂O₃ was deposited on p-Si at 200 °C by atomic layer deposition (ALD) as a high-k gate oxide dielectric (see Experimental Methods and **Figure S8** for measurements of capacitance vs. frequency showing minimal dielectric dispersion). 8 at. % Ga IGO devices were fabricated with the same CLMP method operated at 180 °C on the ~30 nm Al₂O₃ substrates, as shown in **Figure 4a**. **Figure 4b** shows representative transfer characteristics of IGO devices on Al₂O₃ with much steeper switching and a reduced operating voltage range compared to IGO on 100 nm SiO₂, with subthreshold slope values as low as 210 mV/dec and V_{on} around zero. **Figure 4c** shows the excellent output curve current saturation of the high-k IGO devices. The subthreshold slopes for the entire high-k IGO device batch are shown in the histogram in **Figure 4d**. The extracted incremental mobility shows the expected saturation at higher gate fields following the MTR mobility model as shown in **Figure S9**. The device performance comparison for InO_x and IGO devices on 100 nm SiO₂ and IGO on 30 nm Al₂O₃ are tabulated in **Table 1**. The relative variability of device performance metrics such as turn on voltage

Table 1: Summary of TFT device performance

Channel	Von [V]	μ _{lin} [cm ² V ⁻¹ s ⁻¹] (μ _{max})	I_{on}/I_{off}	SS [V/dec]	
180 °C InO _x	-56 ± 4.7	$6.3 \pm 1.6 (9.3)$	10^{4}	11.3 ± 4.97	
180 °C IGO	-24 ± 9.9	$6.1 \pm 3.9 (17.8)$	10^{5}	5.9 ± 4.95	
250 °C annealed IGO	$\textbf{-5.0} \pm 3.2$	$10 \pm 5.6 (22.7)$	10^7	1.1 ± 0.52	
180 °C IGO on Al ₂ O ₃	-0.5 ± 0.8	$2.8 \pm 2.0 \ (6.5)$	10^{5}	0.50 ± 0.22	

and mobility motivates future investigations to improve back-channel passivation in these ultrathin channel devices.

1 2

3

4

5

6

7

8

9

10

11

12

13

14

15

16

17

18

The capability of achieving such steep switching with such a low process temperature is unique to the liquid metal printing process compared with other low-cost methods. Other processes for fabricating metal oxide semiconductors such as solution processing and vacuum-based deposition typically require annealing steps to crystallize the film, whereas the surface oxide that spontaneously forms on the liquid metal is inherently crystalline. Crystalline ALD IGO films can be achieved at temperatures as low as 200 °C in the case of Sheng et al.'s work; however, their maximum reported TFT mobility of 9.45 cm²V⁻¹s⁻¹ was only achieved by annealing at 300 °C.^[59] Hur et al. report ALD IGO TFTs with extremely high mobilities of ~70 cm²V⁻¹s⁻¹, but at the cost of a 400 °C anneal. [60] While vacuum processes can deposit metal oxides at temperatures as low as room temperature, they are inherently limited by the batch-wise nature of loading individual substrates into the deposition chamber, as well as fairly long deposition cycles in the case of ALD. Additionally, the films are typically subjected to a post-deposition anneal at temperatures above most plastic substrate working temperatures. CLMP printing achieves steep switching and mobilities on the order of those produced with vacuum technologies at considerably lower temperatures with no post annealing steps required. Figure 5a illustrates the high mobilities achieved by low-temperature CLMP in the context of the maximum process temperatures of other

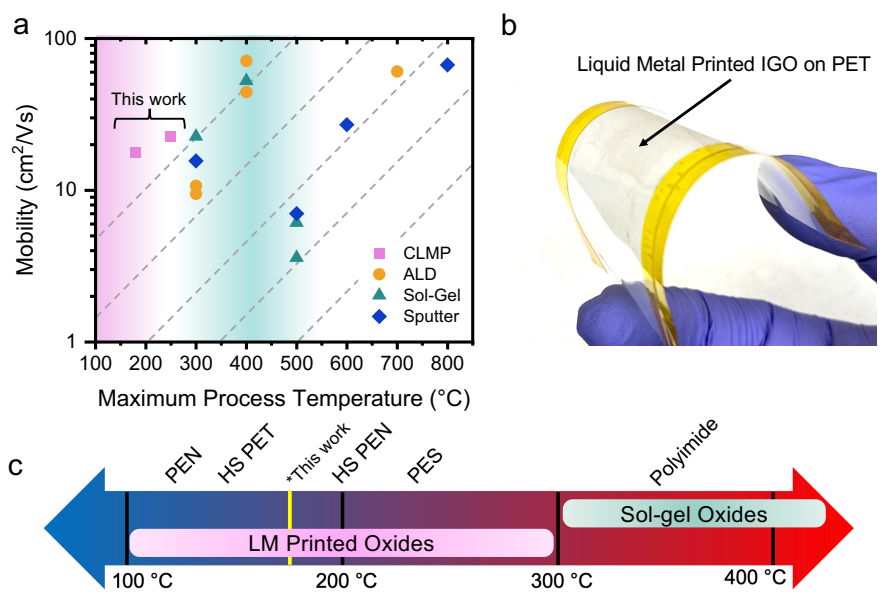


Figure 5: (a) Comparison of mobility vs maximum process temperature of IGO TFTs in literature. (b) Images of IGO deposited on PET demonstrate superior transparency of LMP oxides on flexible substrates. (c) Maximum process temperatures of flexible polymer substrates vs temperature ranges of liquid metal printing and sol-gel processes for fabrication metal oxides (HS denotes heat-stabilized).

IGO TFTs reported in the literature. ^[20-22,32,59-64] Higher electron mobilities above 50 cm²V⁻¹s⁻¹ can be achieved using ALD, sputtering, or sol-gel routes, but the films are typically annealed at temperatures above 300 °C (as high as 800 °C in some cases), rendering them incompatible with flexible substrates. Beyond this downside, the vacuum-based processes like ALD and sputtering require high capital expenditures and are typically batchwise, an inherent limit to throughput.

Figure 5b illustrates the roll-to-roll and plastic substrate compatibility of the CLMP process, producing transparent and flexible IGO printed on PET.

The extension of liquid metal printing to a continuous roller-based process proves to be a facile, low-cost method for high-throughput deposition of high-performance transparent metal oxides on various substrates. This process would be scalable to roll-to-roll processing flows that could print semiconducting films at speeds above 20 cm/s. Additionally, the process temperature is only limited to the thermal constraints of the target substrate and the melting point of the metal used to deposit the oxide. This temperature range can be considered the liquid metal printing "thermal window," as shown in **Figure 5c**. Maximum working temperatures of common flexible plastic substrates are shown, as well as the process temperature ranges of solution processed and liquid metal printed oxides. Depending on the deposition temperature and any postannealing, the CLMP process is compatible with high-temperature resistant polymers such as polyimide down to polyethylene terephthalate (PET).

3. Conclusion

In summary, we present high-performance, liquid metal printed InGaO_x TFTs with the rapid and scalable continuous liquid metal printing (CLMP) method at 180 °C. To the best of our knowledge, this is the lowest process temperature reported so far for liquid metal printed metal oxide TFTs. We have explored the strong Ga surface domination effect and exploited extremely hypoeutectic InGa alloys to achieve Ga-doped crystalline IGO films with reduced oxygen vacancies. We further illustrate the effects of Ga doping through detailed materials characterization, including XRD, UV-Vis, and XPS. With a reduction in the free electron concentration from Ga doping, we fabricate IGO TFTs with up to 25X steeper subthreshold slopes than pure CLMP InO_x TFTs, as well as mobilities up to 18 cm²V⁻¹s⁻¹. We show a further improvement of the steep switching by integration onto high-k Al₂O₃ dielectrics. This record low process temperature enables plastic substrate

1 compatibility, proving CLMP as a low-cost, high-speed, roll-to-roll scalable deposition process

for next-generation transparent flexible high-performance electronics.

3

2

4. Experimental Methods

- 6 Precursor Alloy Preparation: Hypoeutectic InGa alloys were prepared by melting In (Luciteria,
- 7 99.995 %) and Ga (Luciteria, 99.99 %) in a graphite crucible for 10 m at 180 °C in an inert nitrogen
- 8 atmosphere glovebox to minimize surface oxidation. 10, 1, 0.1, 0.01, 0.005, and 0.001 wt. % Ga
- 9 concentrations were prepared by serial dilution of a 10 wt. % Ga sample with In.
- 10 Continuous Liquid Metal Printing: 2D metal oxides were deposited by rolling the liquid metal
- alloy droplet along 3×7 cm substrates at a speed of ~ 5 cm/s with a silicone roller on a hot plate at
- 12 180 °C. The target substrate was treated with ~10 s of atmospheric plasma (Plasma-Etch 1000W
- atmospheric plasma system supplied with 30 LPM compressed dry air) to promote adhesion of the
- printed oxide film. The target substrates were positioned between two dummy substrates to provide
- an area to start and end the deposition process, producing a uniform, continuous metal oxide film
- on the target substrate. The silicone roller was preheated by rolling across Kapton tape on the hot
- plate. The residual liquid metal on the surface of the deposited metal oxide film was wiped with
- isopropyl alcohol (IPA) while still on the hotplate and then again once the sample had cooled to
- 19 room temperature. IGO films printed on PET flexible substrates were printed with the same
- 20 procedure at 180 °C.
- 21 Film Characterization: X-ray photoelectron spectroscopy (XPS) was performed with a Kratos
- 22 Axis Supra XPS at 10⁻⁹ Torr with four printed layers of metal oxide on 100 nm SiO₂ substrates.
- Elemental analysis of the metal oxide films was determined by comparing the Ga 2p, In 3d, and O
- 24 ls peaks. Atomic force microscopy (AFM) was performed with an AIST-NT instrument to
- 25 measure film thickness. UV-Vis was performed with a DeNovix DS-11 FX+ spectrophotometer
- 26 to collect absorbance spectra of single printed layer metal oxide films on glass substrates.
- 27 Transmittance measurements were collected on a Vernier Go Direct SpectroVis Plus
- 28 spectrophotometer with the same single printed layer samples as used for UV-Vis analysis. X-ray
- 29 diffraction (XRD) was performed with a Rigaku MiniFlex diffractometer with Cu Kα radiation
- using a scanning rate of 4° per min on four printed layers of metal oxide on 100 nm SiO₂ substrates.
- 31 Conductivity was determined using four-point probe Van der Pauw resistivity measurements using

- 1 sputtered Au contacts in a 0.5 cm² square geometry at room temperature. Film thickness in **Figures**
- 2 **1h,i** was measured using a Filmetrics F3 spectral reflectometer.
- 3 Device Fabrication: Thin film transistors were fabricated from CLMP metal oxide films printed
- 4 on 100 nm SiO₂ substrates via standard photolithography and wet etching. The channels were
- 5 etched to a dimension of 150 μm in length and 200 μm in width. The 2D InO_x and IGO channels
- 6 were wet etched with 18 % HCl for 2 min. The source drain electrodes were deposited by sputtering
- 7 of ~30 nm thick Au and patterned by liftoff. For low voltage operating devices, 30 nm Al₂O₃ gate
- 8 dielectrics were grown on heavily doped p-Si substrates using an Anric AT-400 atomic layer
- 9 deposition (ALD) tool at 200 °C using trimethylaluminum (TMA) and ozone as precursors. MIM
- structures for measuring gate capacitance were fabricated on identical substrates using circular Au
- pads (0.129 mm²) deposited by sputtering. The frequency-dependent capacitance was measured
- using a Hioki IM 3570 LCR meter from 100 Hz to 1 MHz.
- 13 Device Characterization: The thin film transistor measurements (transfer and output
- characteristics) were taken at room temperature in air with an Agilent E5260A semiconductor
- parameter analyzer. The electronic density of states was extracted from temperature-dependent
- measurements (measured from room temperature to approximately 100 °C) of linear regime, low-
- drain field transfer characteristics. The density of states was extracted via the fitting of a gate-
- voltage dependent activation energy as demonstrated by Zeumault, et al. [65], applying assumptions
- 19 from a multiple trap and release model. NBIS testing was performed at room temperature under a
- 20 white LED light source with a measured intensity of ~3.5 mW/cm². Transfer curves were measured
- using a drain-source voltage $V_{DS} = 1 \text{ V}$ and a gate-source voltage double sweep from $V_{GS} = -40 \text{ V}$
- 22 to +60 V.
- 23 Film Imaging: Optical microscope images were acquired with a Keyence VHX-7100 microscope.
- 24 Supporting Information
- 25 Supporting Information is available from the Wiley Online Library or from the author.
- **26** Conflict of Interest
- 27 The authors declare no conflict of interest.
- 28 Data Availability
- 29 The data that support the findings of this study are available from the corresponding author upon
- 30 reasonable request.
- 31 Acknowledgements

1 This research was supported by the National Science Foundation Electronic and Photonic Materials program (Award #2202501) as well as the National Science Foundation Electronics, 2 Photonics, and Magnetic Devices program (Award #2219991). We acknowledge Paul Defino at 3 Dartmouth College for assistance in AFM scans as well as John Wilderman at the University of 4 New Hampshire for performing XPS measurements. 5 6 7 8 Received: ((will be filled in by the editorial staff)) 9 Revised: ((will be filled in by the editorial staff)) Published online: ((will be filled in by the editorial staff)) 10

References

- 3 [1] R. Fonoll-Rubio, M. Placidi, T. Hoelscher, A. Thomere, Z. J. Li-Kao, M. Guc, V. Izquierdo-4 Roca, R. Scheer, A. Pérez-Rodríguez, *Solar RRL* **2022**, *6*, 2101071.
- 5 [2] P. K. Shihabudeen, A. Roy Chaudhuri, *Sensors and Actuators B: Chemical* **2020**, *305*, 6 127523.
- 7 [3] M. A. Basyooni, Y. R. Eker, M. Yilmaz, Superlattices and Microstructures **2020**, 140, 106465.
- 8 [4] Y. Hara, T. Kikuchi, H. Kitagawa, J. Morinaga, H. Ohgami, H. Imai, T. Daitoh, T. Matsuo, 9 *Journal of the Society for Information Display* **2018**, *26*, 169.
- [5] M. Nag, A. Chasin, M. Rockele, S. Steudel, K. Myny, A. Bhoolokam, A. Tripathi, B. van der
 Putten, A. Kumar, J.-L. van der Steen, J. Genoe, F. Li, J. Maas, E. van Veenendaal, G.
 Gelinck, P. Heremans, *Journal of the Society for Information Display* 2013, 21, 129.
- 13 [6] L. Petti, N. Münzenrieder, C. Vogt, H. Faber, L. Büthe, G. Cantarella, F. Bottacchi, T. D. Anthopoulos, G. Tröster, *Applied Physics Reviews* **2016**, *3*, 021303.
- [7] K.-H. Choi, J.-A. Jeong, J.-W. Kang, D.-G. Kim, J. K. Kim, S.-I. Na, D.-Y. Kim, S.-S. Kim, H.-K.
 Kim, Solar Energy Materials and Solar Cells 2009, 93, 1248.
- 17 [8] K. Nomura, Journal of Information Display 2021, 22, 211.
- 18 [9] R. Hayashi, M. Ofuji, N. Kaji, K. Takahashi, K. Abe, H. Yabuta, M. Sano, H. Kumomi, K. Nomura, T. Kamiya, M. Hirano, H. Hosono, *Journal of the Society for Information Display* 2007, 15, 915.
- 21 [10] Y. Magari, T. Kataoka, W. Yeh, M. Furuta, *Nat Commun* **2022**, *13*, 1078.
- 22 [11] H. Hosono, *Journal of Non-Crystalline Solids* **2006**, *352*, 851.
- 23 [12] M. Mizuhashi, Thin Solid Films 1980, 70, 91.
- 24 [13] C. C. Wu, C. I. Wu, J. C. Sturm, A. Kahn, Applied Physics Letters 1997, 70, 1348.
- 25 [14] K. Nomura, H. Ohta, A. Takagi, T. Kamiya, M. Hirano, H. Hosono, *Nature* **2004**, *432*, 488.
- [15] W. J. Scheideler, R. Kumar, A. R. Zeumault, V. Subramanian, *Advanced Functional Materials* 27 2017, 27, 1606062.
- [16] R. S. Datta, N. Syed, A. Zavabeti, A. Jannat, M. Mohiuddin, M. Rokunuzzaman, B. Yue
 Zhang, M. A. Rahman, P. Atkin, K. A. Messalea, M. B. Ghasemian, E. D. Gaspera, S.
 Bhattacharyya, M. S. Fuhrer, S. P. Russo, C. F. McConville, D. Esrafilzadeh, K. Kalantar-
- 31 Zadeh, T. Daeneke, *Nat Electron* **2020**, *3*, 51.
- 32 [17] N. Cabrera, N. F. Mott, Rep. Prog. Phys. **1949**, *12*, 163.
- [18] T. Daeneke, K. Khoshmanesh, N. Mahmood, I. A. De Castro, D. Esrafilzadeh, S. J. Barrow,
 M. D. Dickey, K. Kalantar-zadeh, *Chem. Soc. Rev.* 2018, 47, 4073.
- 35 [19] A. B. Hamlin, Y. Ye, J. E. Huddy, M. S. Rahman, W. J. Scheideler, *npj 2D Mater Appl* **2022**, *6*, 36 1.
- 37 [20] Y. G. Kim, T. Kim, C. Avis, S.-H. Lee, J. Jang, *IEEE Transactions on Electron Devices* **2016**, *63*, 38 1078.
- 39 [21] C.-H. Choi, Y.-W. Su, L.-Y. Lin, C.-C. Cheng, C. Chang, RSC Advances **2015**, *5*, 93779.
- 40 [22] H. J. Yang, H. J. Seul, M. J. Kim, Y. Kim, H. C. Cho, M. H. Cho, Y. H. Song, H. Yang, J. K. Jeong, *ACS Appl. Mater. Interfaces* **2020**, *12*, 52937.
- 42 [23] M. Jia, J. T. Newberg, J. Phys. Chem. C 2019, 123, 28688.
- 43 [24] Z. J. Farrell, C. Tabor, *Langmuir* **2018**, *34*, 234.

- 1 [25] Z. J. Farrell, A. R. Jacob, V. K. Truong, A. Elbourne, W. Kong, L. Hsiao, M. D. Dickey, C. Tabor, *Chem. Mater.* **2023**, *35*, 964.
- 3 [26] A. Koh, R. Mrozek, G. Slipher, *Adv Materials Inter* **2018**, *5*, 1701240.
- 4 [27] A. Zavabeti, J. Z. Ou, B. J. Carey, N. Syed, R. Orrell-Trigg, E. L. H. Mayes, C. Xu, O. Kavehei, A. P. O'Mullane, R. B. Kaner, K. Kalantar-zadeh, T. Daeneke, *Science* **2017**, *358*, 332.
- 6 [28] Y. Ye, A. B. Hamlin, J. E. Huddy, M. S. Rahman, W. J. Scheideler, *Advanced Functional Materials* **2022**, *32*, 2204235.
- 8 [29] A. B. Hamlin, S. A. Agnew, J. C. Bonner, J. W. P. Hsu, W. J. Scheideler, *Nano Lett.* **2023**, *23*, 2544.
- 10 [30] A. Martin, M. Thuo, *ACS Nano* **2024**, *18*, 6740.
- [31] J. Guo, J. Li, S. Ze, F. Li, J. Wang, Q. Liu, Z. Hua, L. Yang, F. Liu, B. Liu, *Applied Surface* Science 2024, 160131.
- 13 [32] L. Ji, X. Chen, X. Su, J. Wan, Z. Tu, H. Wu, C. Liu, *Applied Physics Letters* **2023**, *122*, 202105.
- 14 [33] J. Qi, J. F. Liu, Y. He, W. Chen, C. Wang, Journal of Applied Physics **2011**, 109, 063520.
- 15 [34] H. S. Kim, P. D. Byrne, A. Facchetti, T. J. Marks, *J. Am. Chem. Soc.* **2008**, *130*, 12580.
- 16 [35] H. Pu, Q. Zhou, L. Yue, Q. Zhang, Semicond. Sci. Technol. 2013, 28, 105002.
- 17 [36] Y. Li, D. Zhu, W. Xu, S. Han, M. Fang, W. Liu, P. Cao, Y. Lu, *Journal of Materials Chemistry C* **2020**, *8*, 310.
- 19 [37] K. Irmscher, M. Naumann, M. Pietsch, Z. Galazka, R. Uecker, T. Schulz, R. Schewski, M. Albrecht, R. Fornari, *physica status solidi (a)* **2014**, *211*, 54.
- 21 [38] S. Guo, W. Diyatmika, Y. Unutulmazsoy, L. Yang, B. Dai, L. Xu, J. Han, V. Ralchenko, A. Anders, J. Zhu, *Applied Surface Science* **2022**, *585*, 152604.
- [39] J. Yao, N. Xu, S. Deng, J. Chen, J. She, H.-P. D. Shieh, P.-T. Liu, Y.-P. Huang, *IEEE Transactions on Electron Devices* **2011**, *58*, 1121.
- [40] S. Guo, L. Yang, X. Zhang, B. Dai, F. Geng, Z. Yang, P. Wang, G. Gao, L. Xu, J. Han, V.
 Ralchenko, J. Zhu, *Ceramics International* **2019**, *45*, 21590.
- [41] F. He, Y. Qin, Y. Wang, Z. Lin, J. Su, J. Zhang, J. Chang, Y. Hao, *IEEE Journal of the Electron Devices Society* **2021**, *9*, 373.
- 29 [42] F. Jaehnike, D. V. Pham, C. Bock, U. Kunze, J. Mater. Chem. C 2019, 7, 7627.
- [43] J. W. Hennek, J. Smith, A. Yan, M.-G. Kim, W. Zhao, V. P. Dravid, A. Facchetti, T. J. Marks, *J. Am. Chem. Soc.* 2013, *135*, 10729.
- [44] Y. Gassenbauer, R. Schafranek, A. Klein, S. Zafeiratos, M. Hävecker, A. Knop-Gericke, R.
 Schlögl, *Phys. Rev. B* 2006, *73*, 245312.
- [45] K. Jeon, C. Kim, I. Song, J. Park, S. Kim, S. Kim, Y. Park, J.-H. Park, S. Lee, D. M. Kim, D. H.
 Kim, Applied Physics Letters 2008, 93, 182102.
- 36 [46] K. Nomura, T. Kamiya, H. Ohta, T. Uruga, M. Hirano, H. Hosono, *Phys. Rev. B* **2007**, *75*, 035212.
- 38 [47] R. Khanal, D. B. Buchholz, R. P. H. Chang, J. E. Medvedeva, *Phys. Rev. B* **2015**, *91*, 205203.
- 39 [48] Sungsik Lee, Sanghun Jeon, A. Nathan, J. Display Technol. 2013, 9, 883.
- 40 [49] L. Li, N. Lu, M. Liu, *IEEE Electron Device Letters* **2014**, *35*, 226.
- 41 [50] J.-H. Na, J.-H. Park, W. Park, J. Feng, J.-S. Eun, J. Lee, S.-H. Lee, J. Jang, I. M. Kang, D.-K. Kim, J.-H. Bae, *Nanomaterials* **2024**, *14*, 466.
- 43 [51] H. Oh, S.-M. Yoon, M. K. Ryu, C.-S. Hwang, S. Yang, S.-H. K. Park, *Applied Physics Letters* **2011**, *98*, 033504.

- 1 [52] H. Oh, S.-M. Yoon, M. K. Ryu, C.-S. Hwang, S. Yang, S.-H. K. Park, *Applied Physics Letters* **2010**, *97*, 183502.
- 3 [53] Y. Kim, C. Kim, J. Mater. Chem. C 2023, 11, 7121.
- 4 [54] W.-S. Kim, Y.-H. Lee, Y.-J. Cho, B.-K. Kim, K. T. Park, O. Kim, *ECS J. Solid State Sci. Technol.* **2016**, *6*, Q6.
- [55] B. S. Kim, Y. Taek Jeong, D. Lee, T. Choi, S.-H. Jung, J. Whan Choi, C. Yang, K. Jo, B. Lee, E.
 Park, D. Na Kim, Y. Kim, S. Shin, *Applied Physics Letters* 2013, 103, 072110.
- 8 [56] W. Li, C. Gao, X. Li, J. Yang, J. Zhang, J. Chu, *Microelectronic Engineering* **2024**, *286*, 9 112142.
- 10 [57] K. Ide, K. Nomura, H. Hosono, T. Kamiya, *physica status solidi (a)* **2019**, *216*, 1800372.
- [58] C. Zhang, B. F. Yang, D. Wang, Z. Y. Zhou, C. Y. Han, L. X. Qian, P. T. Lai, X. D. Huang, *IEEE Trans. Electron Devices* **2023**, *70*, 4958.
- 13 [59] J. Sheng, E. J. Park, B. Shong, J.-S. Park, *ACS Appl. Mater. Interfaces* **2017**, *9*, 23934.
- [60] J. S. Hur, M. J. Kim, S. H. Yoon, H. Choi, C. K. Park, S. H. Lee, M. H. Cho, B. J. Kuh, J. K. Jeong,
 ACS Appl. Mater. Interfaces 2022, 14, 48857.
- [61] J. H. Park, W. J. Choi, S. S. Chae, J. Y. Oh, S. J. Lee, K. M. Song, H. K. Baik, *Jpn. J. Appl. Phys.* 2011, 50, 080202.
- [62] H. Q. Chiang, D. Hong, C. M. Hung, R. E. Presley, J. F. Wager, C.-H. Park, D. A. Keszler, G. S.
 Herman, Journal of Vacuum Science & Technology B: Microelectronics and Nanometer
 Structures Processing, Measurement, and Phenomena 2006, 24, 2702.
- 21 [63] R. E. Presley, D. Hong, H. Q. Chiang, C. M. Hung, R. L. Hoffman, J. F. Wager, *Solid-State Electronics* **2006**, *50*, 500.
- 23 [64] Young Hwan Hwang, Byeong-Soo Bae, J. Display Technol. 2013, 9, 704.

26 27

[65] A. Zeumault, W. Scheideler, V. Subramanian, Advanced Functional Materials 2017, 27,
 1701021.

1 Supporting Information

Hypoeutectic liquid metal printing of two-dimensional indium gallium oxide transistors

Simon A. Agnew, Anand P. Tiwari, Samuel W. Ong, Md Saifur Rahman, and William J. Scheideler*

- Thayer School of Engineering
- 8 Dartmouth College, Hanover, NH 03755, United States
- 9 E-mail: william.j.scheideler@dartmouth.edu

Keywords: liquid metals, 2D oxides, transparent electronics, thin film transistors, flexible transistors

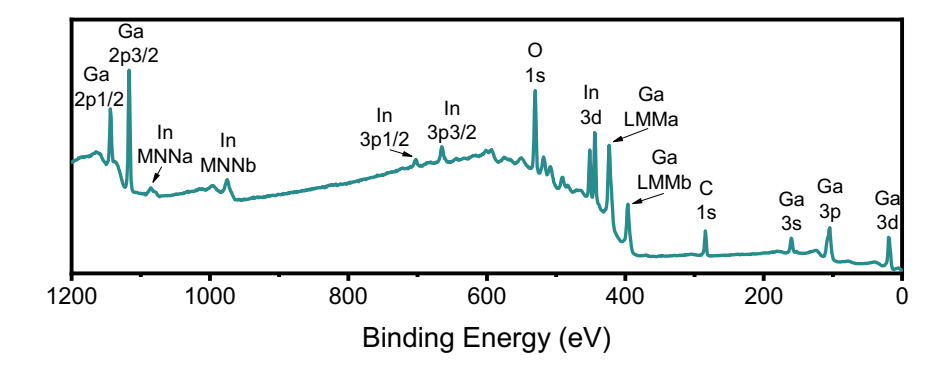


Figure S1: XPS wide survey scan of IGO film sample containing 63 at. % Ga.

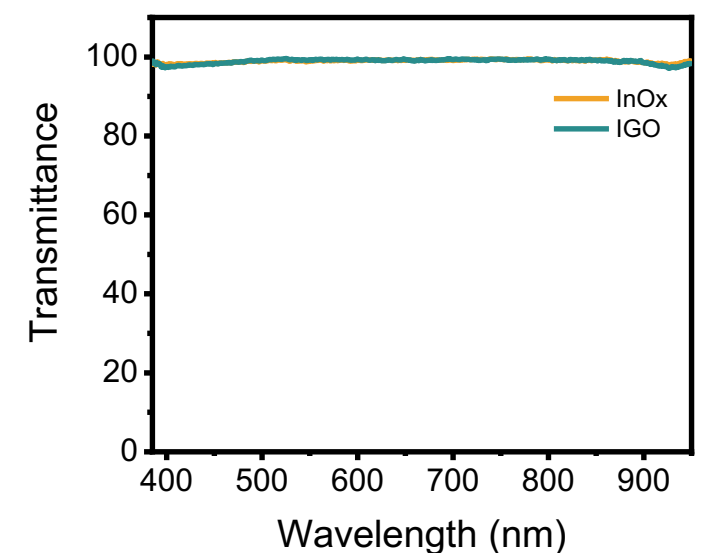
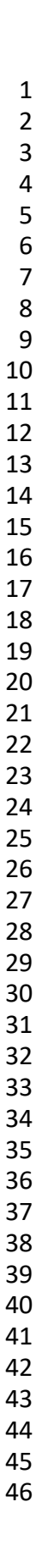


Figure S2: Transmittance plot of pure InO_x and 8 at. % Ga IGO.



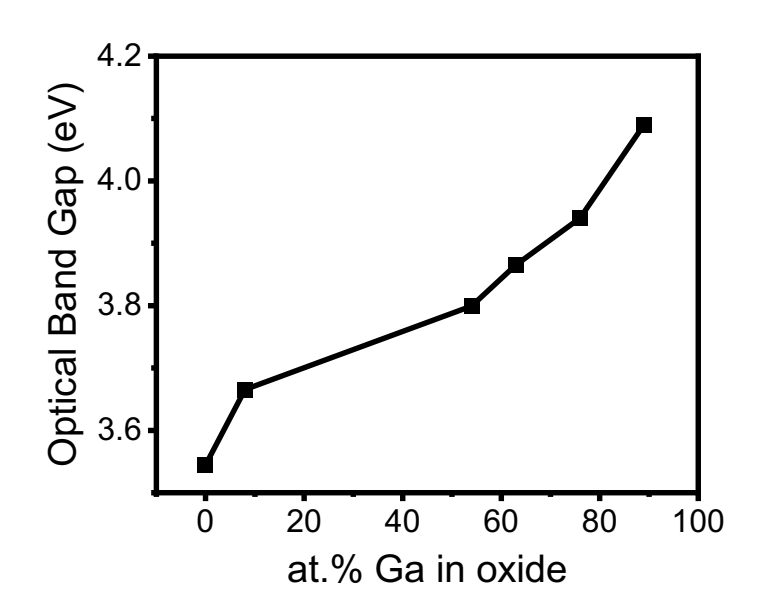


Figure S3: Optical band gap versus Ga content in the oxide.

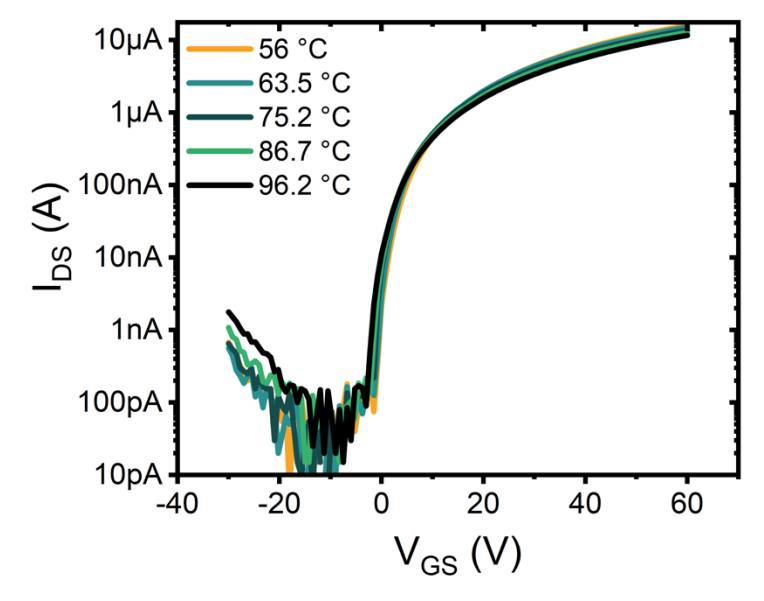
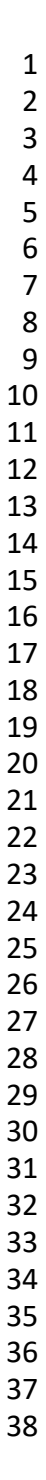


Figure S4: Transfer curves of IGO device used for total DOS extraction measured at various temperatures in open air. $V_{DS} = 1$ V. Minimal shifting of V_{on} and I_{on} occurred.



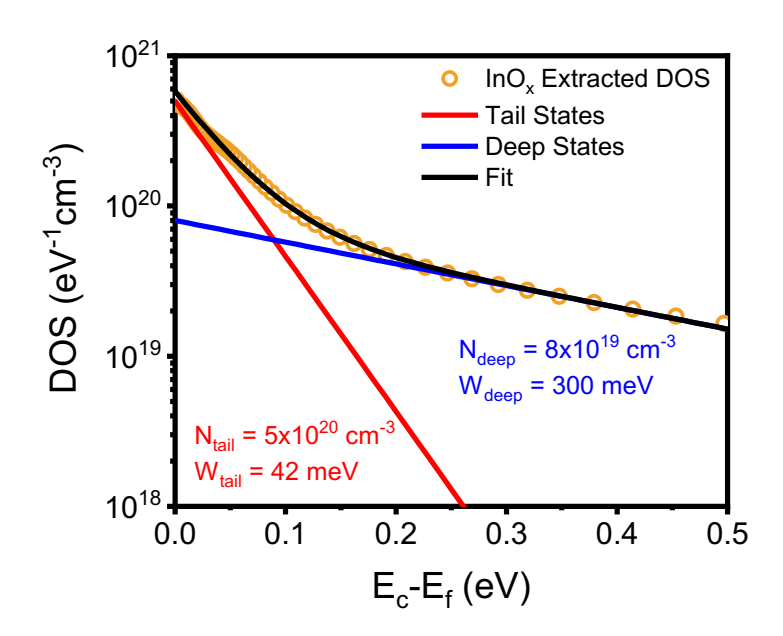


Figure S5: Biexponential DOS distribution fit for extracted InO_x DOS.

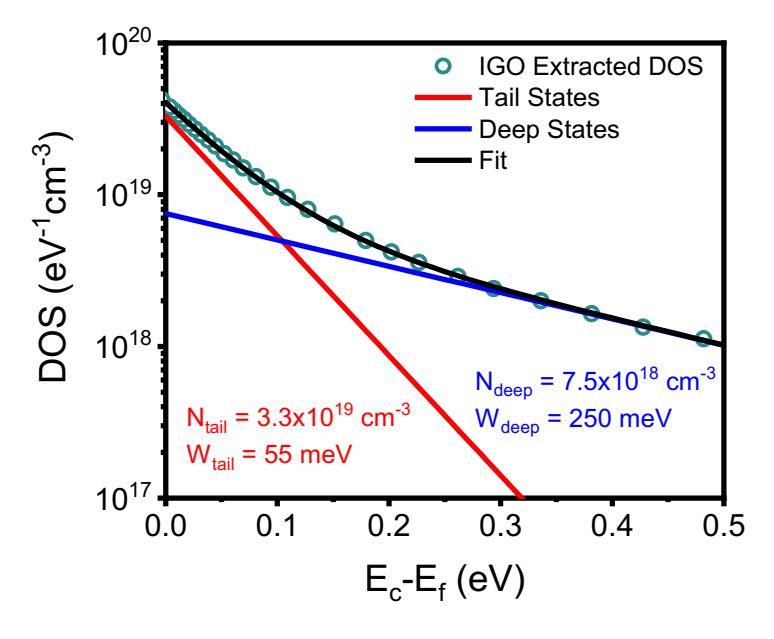


Figure S6: Biexponential DOS distribution fit for extracted IGO DOS.



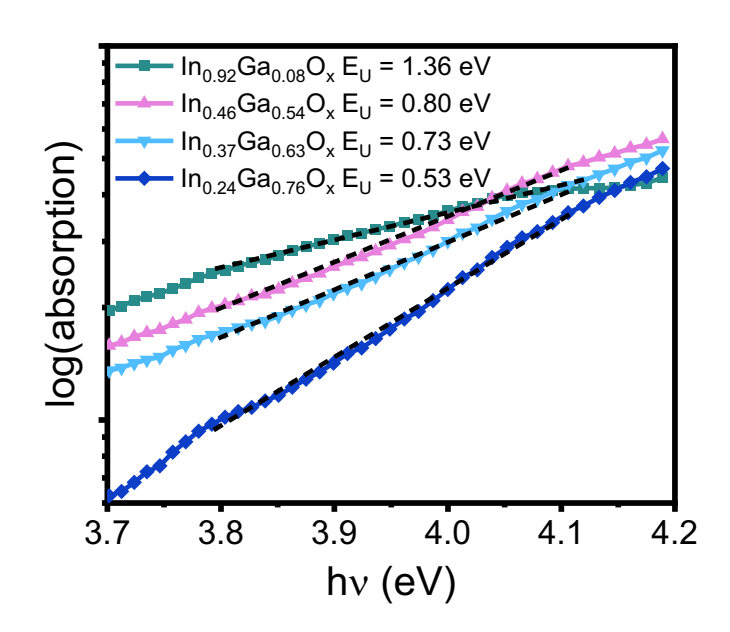


Figure S7: Absorption edge of IGO films indicating a steeper Urbach tail slope as Ga content increases.

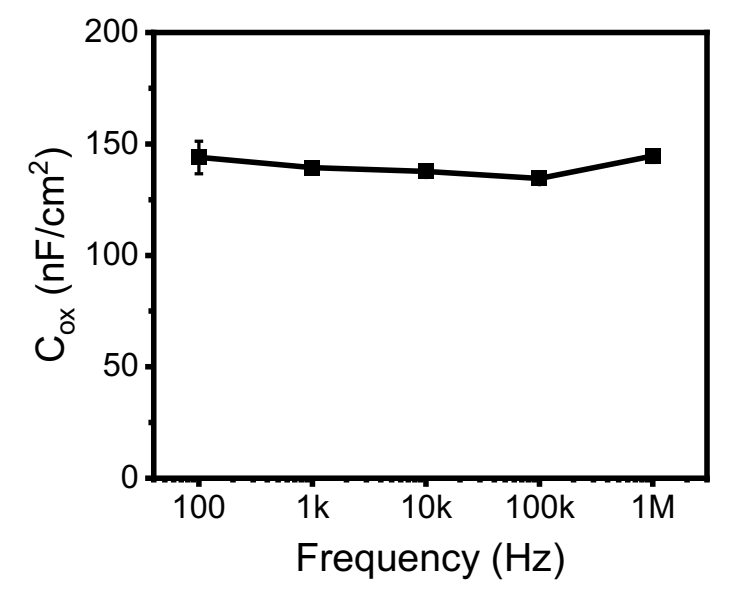


Figure S8: Capacitance per area of 30 nm ALD Al₂O₃ dielectric capacitance as measured with sputtered Au contact metal-insulator-metal (MIM) capacitor structures on a highly doped Si wafer.



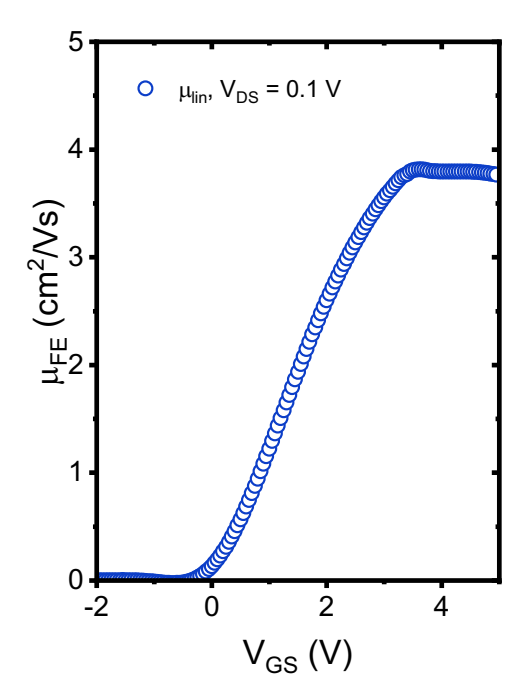


Figure S9: Incremental field-effect mobility of IGO devices on 30 nm Al₂O₃ dielectrics.